

DETC2013-13132

**AN MRI COIL-MOUNTED MULTI-PROBE ROBOTIC POSITIONER FOR
CRYOABLATION**

Faye Y. Wu

Mechanical Engineering Department
Massachusetts Institute of Technology
Cambridge, MA, USA

Meysam Torabi

Wyss Institute for Biologically Inspired Engineering
School of Engineering and Applied Sciences
Harvard University
Cambridge, MA, USA

Atsushi Yamada

Department of Radiology
Brigham and Women's Hospital
Boston, MA, USA

Alex Golden

School of Engineering and
Applied Sciences
Harvard University
Cambridge, MA, USA

Gregory S. Fischer

Mechanical Engineering
Department
Worcester Polytechnic Institute
Worcester, MA, USA

Kemal Tuncali, M.D.

Department of Radiology
Brigham and Women's Hospital
Boston, MA, USA

Dan D. Frey

Mechanical Engineering
Department
Massachusetts Institute of
Technology
Cambridge, MA, USA

Conor Walsh

Wyss Institute for Biologically
Inspired
Engineering
School of Engineering and
Applied Sciences
Harvard University
Cambridge, MA, USA

ABSTRACT

Cryoablation is a percutaneous procedure for treating solid tumors using needle-like instruments. This paper presents an interventional guidance device for faster and more accurate alignment and insertion of multiple probes during cryoablation performed in closed bore magnetic resonance (MR) imaging systems. The device is compact and is intended to be mounted onto a Siemens 110 mm MR loop coil. A cable-driven two-degrees-of-freedom spherical mechanism mimics the wrist motion as it orients the intervention probes about a remote center of motion located 15 mm above the skin. A carriage interfaces with the probes via a thumbscrew-fastened latch to passively release the probes from their tracks, enabling them to be inserted sequentially and freeing them to move with respiration. Small actuator modules containing piezoelectric encoder-based motors are designed to be snap-fit into the device for ease of replacement and sterilization. The robot MRI compatibility was validated with standard cryoablation

imaging sequences in 3T MR environment, yielding a maximum of 4% signal to noise ratio during actuator motion. Bench-level device characterization demonstrated a maximum error of 0.78° in the carriage movement. Needle-tip placement experiments for multiple targets in gelatin were performed using our image-guided navigation software, measuring an average targeting error of 2.0 mm.

INTRODUCTION

Cryoablation, a minimally invasive procedure, treats soft tissue cancer found in the lung, liver, breast, kidney and prostate through the precise placement of liquid nitrogen or pressurized argon gas filled probes [1]. Recent interventional cryoablation studies reported almost 100% efficacy for the treatment of small renal tumors (≤ 4 cm) [2, 3]. This method is less painful, has lower risk of developing metastatic disease and requires fewer retreatments than radiofrequency ablation [4-6].

Cryoablation is often performed in conjunction with Magnetic Resonance Imaging (MRI) to track the position of ablation probes, as well as to visualize the ice ball formation for direct comparison between the kill zone and the tumor margin. After interventionists determine the location of a lesion with an initial scan, they would approximate an entry site for the probe on the surface of the skin and make a small incision at the entry site to facilitate insertion. The imaging data is used to estimate the desired compound entry angle and the probe is inserted in an iterative manner, a few centimeters at a time, each time checking its trajectory with MR scans, until the tip reaches the desired endpoint inside the patient. Given the limited space within an MRI machine, the manual insertion and adjustment of the intervention probe must be conducted outside the imaging bore. The interventionist must compromise between efficiency and precision, as each scan and adjustment necessitates sliding the patient into and out of the bore. Additionally, the simultaneous use of multiple probes is usually needed to create a synergistic ice formation that encompasses the entire tumor and ensure the tumor reaches the minimal required ablation temperature of -40°C [7-9]. Due to the challenges in precisely calculating the desired entry angle and subsequently inserting the needle along it, more than half of the procedure time may be spent correcting probe path [10]. Similarly, inserting the probe precisely along its planned path was also observed to be the most time-intensive portion of the operation for many CT-guided interventions [11].

To solve the probe alignment challenge, a number of devices have been developed in recent years. Taillant et al. [12] and Hata et al. [13] introduced MRI compatible systems that mount on the scanner bed and suspend over the patient. The breast biopsy and intervention apparatus presented by Larson et al. [14] uses telescopic rods to situate probes while keeping ultrasonic actuators away from the imaging bore to minimize any distortion effects to the MR images. Kokes et al. [15] reported another MRI compatible needle driver for breast tumor radiofrequency ablation, which employs a haptic device to remotely control the robot. Rasmus et al. [16], Muntener et al. [17] and Su et al. [18] developed bed-mounting robotic mechanisms that targeted single probe treatment of the prostate gland. Walsh et al. [19] designed a compact device that attaches directly to the patient via adhesive pads and orients a single probe for CT and ultrasound-image-guided biopsy.

The available technologies for placing probes are either large plus expensive or designed to work with single probe ablation only. Furthermore, unique to MR-image-guided procedures, a flexible imaging coil must be affixed to the patient over the region of interest to capture radio frequency data coming from the body and produce high quality images. Many mechanisms designed for CT or ultrasound-image-guided procedures cannot accommodate imaging coil placements, limiting their possibilities of redesigning for MR-guided operations.

Therefore, there is a clear opportunity for an inexpensive, small footprint MRI-compatible system that mounts directly to

the imaging coil and enables rapid, precise and accurate guidance for multiple probes. This paper presents the design and evaluation of such a system. The device is designed primarily for cryoablation performed in the abdominal area, where multiple probes are required, but it can also be used for other image-guided percutaneous instrument insertions.

DEVICE DESIGN

The robot presented in this paper is designed to work for the most common clinical case, where three 17-gauge probes (1.473 mm in diameter and 17.5 cm long) are placed, sharing the approximate same probe insertion site on the skin, to reach an average depth of 125 mm and maximum tilt of $\pm 45^{\circ}$. Typically, the tumor is 25-30 mm in diameter.

Mechanism Design Concept

The form factor of the device was greatly influenced by the procedure work-flow and the ease of sterilization. It was determined that a total of three degrees of freedom (DOFs) are essential in the placement of multiple intervention probes: two actuated DOFs for orienting the probe and one passive DOF for releasing the probe from a guide after insertion. The action of inserting the probe was decided to be performed manually to ensure safety of the patient. Utilizing the device and corresponding navigation software to set the angle of insertion, the interventionist can accurately position the probes without performing multiple scans. To optimally utilize the small workspace inside a closed bore, a coil-mounted system that places up to three cryoablation probes was designed as shown in Fig. 1.

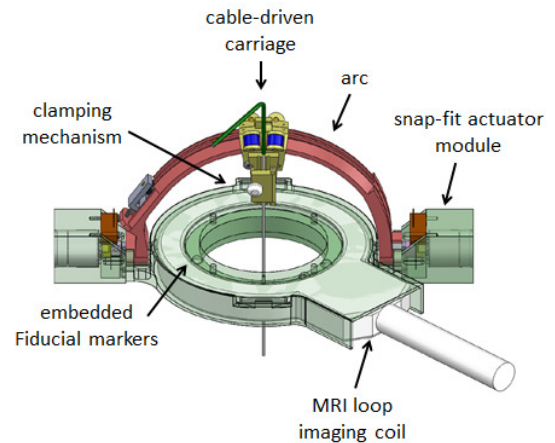


Figure 1. THE DEVICE CONTAINS TWO ACTUATED DOFS FOR ORIENTING THE PROBE AND ONE MANUALLY CONTROLLED DOF FOR RELEASING THE PROBE. THE HOLLOW ROUND BASE ENABLES THE DEVICE TO BE MOUNTED TO AN IMAGING COIL AND ALLOWS THE PHYSICIAN TO HAVE ACCESS TO THE INSERTION SITE.

Typically, the device and the enclosed imaging coil are mounted on the patient with straps or adhesive pads. The probes are placed one at a time, as shown in Fig. 2. The arc and

carriage move to the first position, allowing the probe inside the first track to be inserted manually. The probe can then be released simply by opening the clamping mechanism and actuating the arc to the next position to guide the newly placed probe in the second track. The arc should always rotate in the same direction to avoid colliding with previously placed probes, and the software driving the device assists the user with managing the order of probe placement. Key design features are addressed below and more details can be found in [20].

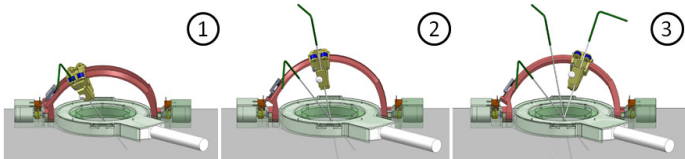


Figure 2. PROBES ARE PLACED SEQUENTIALLY AND LEFT IN PLACE.

Spherical Mechanism

Mimicking the wrist motion, a spherical mechanism consisting of an arc and a carriage was chosen to describe the two angular DOFs of the probe. The two components' axes of rotation are coplanar; their intersection point is the RCM and is positioned as close as possible to the preselected probe insertion point, which in the current prototype is 15 mm above the skin surface due to actuator size, to minimize the length of the entry site incision.

The motion of the carriage is constrained by a custom-designed roller bearing. Since a small misalignment between the carriage and arc would amplify error at the probe tip, the appropriate bearing stiffness was designed and tested not only to enable smooth, low friction motion, but also to decrease backlash and other undesired movement. As shown in Fig. 3, the arc profile is trapezoidal. Five rollers, four on the top and one on the bottom, are preloaded onto the sides of the arc. The walls of the carriage are offset from the surface of the arc by 1.5 mm, avoiding sliding friction caused by direct contact.

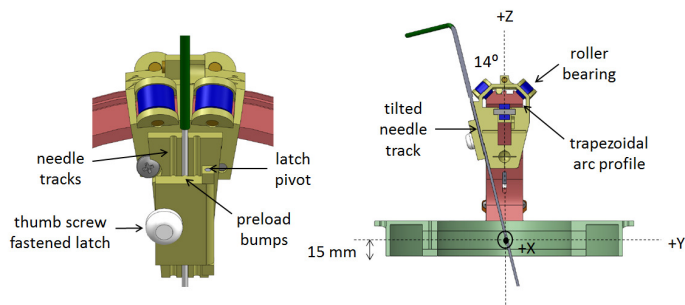


Figure 3. THREE TRACKS ON THE CARRIAGE SEPARATE THE PROBES TO PREVENT THEM FROM INTERSECTING AT RCM. A THUMBSCREW AND LATCH COMBINATION IS USED TO PRELOAD AND LOCK THE PROBES IN THE CARRIAGE. THE CUSTOM-DESIGNED ROLLER BEARING CONSTRAINS THE MOTION OF THE CARRIAGE AND MINIMIZES FRICTION.

Hertz contact stress between the roller and the surface of the arc was calculated to prevent significant pitting or fatigue at the contact surfaces. Small and wide rubber rollers were selected to increase the contact area, decrease maximum contact stress on the rollers, and improve traction. The outer diameter of the roller is three times the diameter of the dowel pin holding it in the carriage, allowing the roller to rotate easily on the pin without losing excess energy from its sliding contact with the pin [21]. This is important in reducing the torque and power requirements of the actuators. Bench level experiment conducted with a Logger Pro force sensor (Vernier Software and Technology, Beaverton, OR) showed that a maximum force of 2.71 N, with a standard deviation of 0.01 N, is required to move the carriage along the arc.

The probes are secured to the carriage from the side, allowing them to be easily disengaged from the carriage as the arc rotates clockwise about the x-axis. A thumb screw fastens a door-like latch on the carriage, locking the probes in place with friction and compression. As mentioned earlier, the three needle tracks, spaced 3 mm apart, prevent the probes from intersecting at the RCM while maintaining the 2-DOF spherical movement. The tracks are tilted 14° to direct the probes toward the x-axis, as illustrated in Fig. 3.

Actuation and Cable Based Transmission

Piezo LEGS rotatory motors (Piezomotor, Sweden) were selected for this device due to the small size, large torque capacity, low image distortion, low friction and ease of position control compared to other MRI compatible actuators, such as Shinsei ultrasonic motor [22], pneumatics [23] and hydraulics [24]. Encoder modules were obtained (US Digital, Vancouver, WA) to perform closed loop control.

Actuators and the associated electronics are difficult to clean with conventional sterilization processes, thus they were designed to be enclosed in a single removable casing that snaps into the remainder of the device (Fig. 4). The square end of the extension shaft, along with the peg-in-hole feature in the casing,

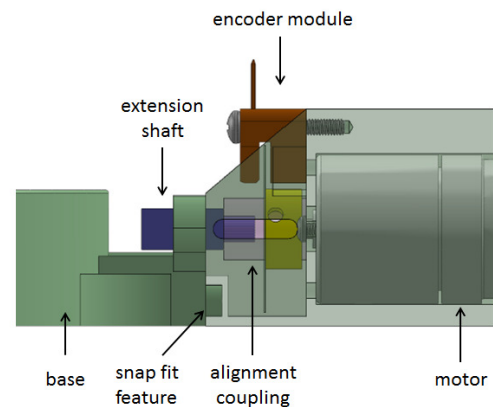


Figure 4. REPLACEABLE MOTOR MODULES ENCLOSE ELECTRONICS THAT ARE DIFFICULT TO STERILIZE AND SNAP-FIT INTO THE BASE.

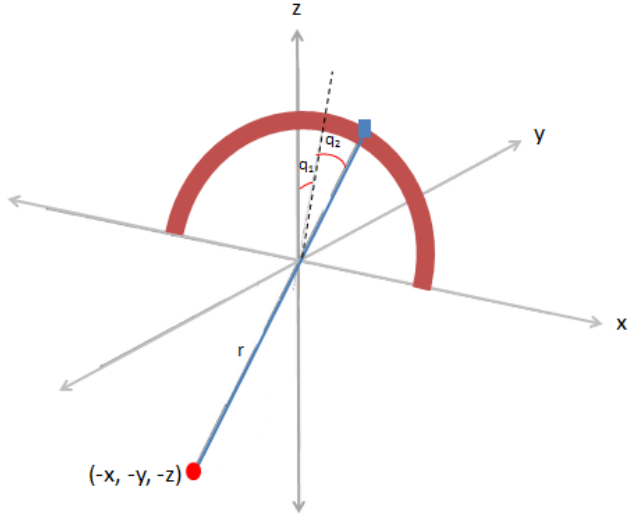


Figure 8. A SIMPLE MODEL USED TO REPRESENT THE DEVICE COORDINATE SYSTEM. THE SEMICIRCLE IS THE ARC, THE SQUARE IS THE CARRIAGE, THE DOT IS THE TARGET, AND THE SOLID LINE IS THE PROBE.

For the kinematics of the actual mechanism, 14° needs to be added to q_1 due to the tilt of the needle tracks, and for q_2 , a compensation angle is needed for probes placed in different tracks. Demonstrated in Fig. 9a, if a probe in track 2 (left dotted line) coincides with the target, then the probe in track 3 (right dotted line) needs to rotate clockwise by δq_2 to reach the target (lower solid line). Similarly, a probe in track 1 needs to rotate counterclockwise by δq_2 to reach the target (Fig. 9b). It can also be seen that by separating the probes into different tracks, they do not intersect at the origin (RCM). Here, track 1 is defined as the left most track, track 3 as the right most track, and track 2 as the middle track, which also intersects the RCM.

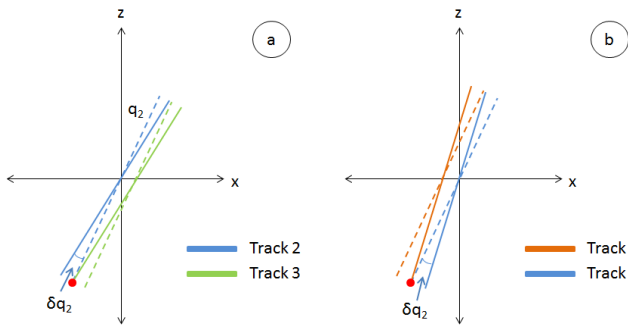


Figure 9. ANGLE COMPENSATION IS NEEDED FOR PROBES PLACED IN TRACKS OTHER THAN THE ONE IN THE MIDDLE (TRACK 2).

The compensation angle can be found from

$$\delta q_2 = \tan^{-1}\left(\frac{d}{r}\right) \quad (2)$$

where d is the distance between the needle tracks (3 mm). Taking into account the ratio between the radius of the driving pulley and the radius of the arc, as well as change in the absolute position of the cable as the arc moves, the amount of motor rotation needed to drive the carriage can be determined. The inverse kinematics relating the target coordinates to the motor angles are

$$q_{m1} = \tan^{-1}\left(\frac{y}{z}\right) + 14 \quad (3)$$

$$q_{m2} = [q_2 + (\text{track} - 2)\delta q_2] \frac{r_{\text{arc}}}{r_{\text{pulley}}} - |q_1' - q_1| \quad (4)$$

where r_{arc} is 80 mm, r_{pulley} is 7 mm, and $|q_1' - q_1|$ is the change of arc position.

A MATLAB script with graphical output (Fig. 10) was written to simulate the operation of the device and verify the above kinematics equations. Targets can either be generated or defined by the user based on known physical conditions of cryoablation. A simple sorting function reorders the target points to maintain clockwise arc rotation and prevent the arc from colliding with previously placed probes. The inverse kinematics is adjusted to allow the probe in track 1 to reach the first target, probe in track 2 to reach the second target, and so forth. The minimum distances between the probes are calculated to ensure that the probes do not intersect with one another.

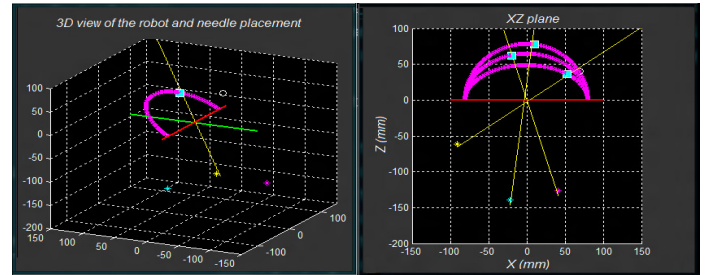


Figure 10. THE MATLAB SCRIPT SIMULATES DEVICE OPERATION AND VERIFIES KINEMATICS. THE MINIMUM DISTANCES BETWEEN THE PROBES ARE CALCULATED TO ENSURE THEY DO NOT INTERSECT AT THE RCM.

PROTOTYPING AND CONTROL IMPLEMENTATION

The device was 3D printed with ABS (Objet Ltd., Rehovot, Israel) with a view that it could be manufactured at a larger scale using injection molding. Figure 11 shows the prototype with three probes clamped in the needle guide.

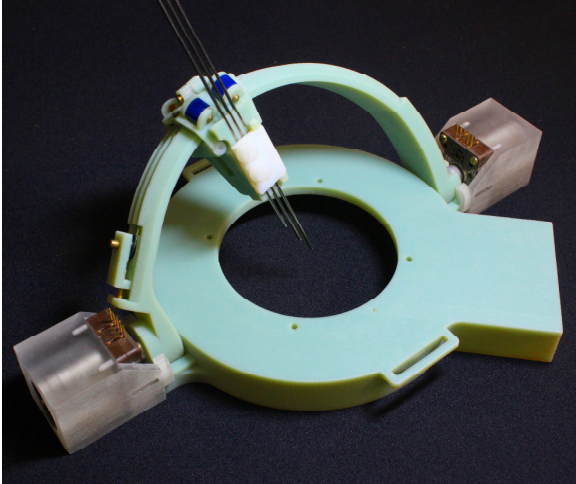


Figure 11. 3D PRINTED DEVICE PROTOTYPE SHOWN WITH THREE PROBES ATTACHED.

Figure 12 is a screenshot of the navigation software developed as a 3D Slicer Image-Guided-Therapy (IGT) module to perform device registration and calibration, plan probe trajectory, and visualize robot movement. As discussed earlier, the uniquely positioned fiducials help with transforming selected targets from the MR image coordinates to the robot coordinates. The target coordinates are then sent to a Java program via the navigation software to calculate inverse kinematics. This Java program runs on a computer in the control room, which in turn communicates with the MRI compatible robot controller placed inside the scanning room through fiber optic cables. Since the controller is completely shielded, it allows the motor to move during a scan without compromising image quality [26]. A PID controller uses the encoder data to perform closed loop position control and guides the robot to the commanded position. The encoder data is also converted to target positions with forward kinematic equations in the Java program, allowing the corresponding virtual probe and robot positions to be displayed as part of the graphical user interface. The software system architecture is shown in Fig. 13.

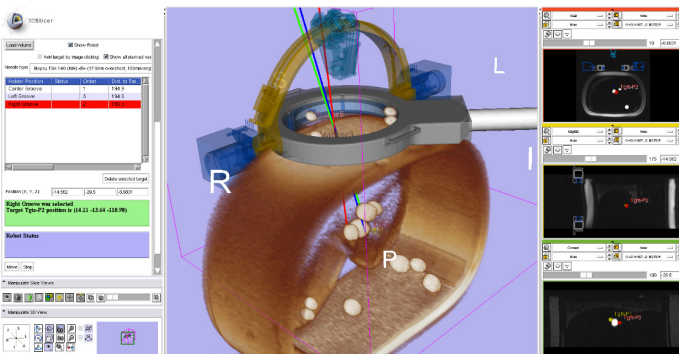


Figure 12. AN IMAGE-GUIDED NAVIGATION SOFTWARE WAS DEVELOPED IN 3D SLICER FOR DEVICE REGISTRATION AND PROBE PATH VISUALIZATION.

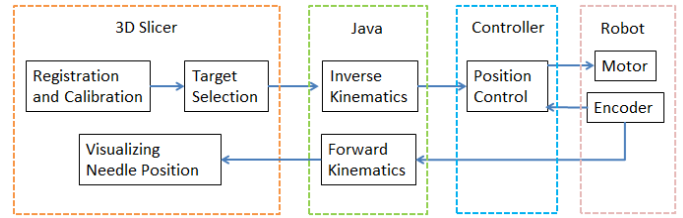


Figure 13. BLOCK DIAGRAM OF SOFTWARE SYSTEM ARCHITECTURE.

SYSTEM EVALUATION

MRI compatibility was evaluated in a Siemens 3T Verio MR Scanner with the robot placed on top of a Supertech Interventional 3D Abdominal Phantom (Elkhart, IN). As shown in Fig. 14, the controller was placed approximately 3 m from the imaging bore, powered and grounded by an in-room AC outlet.

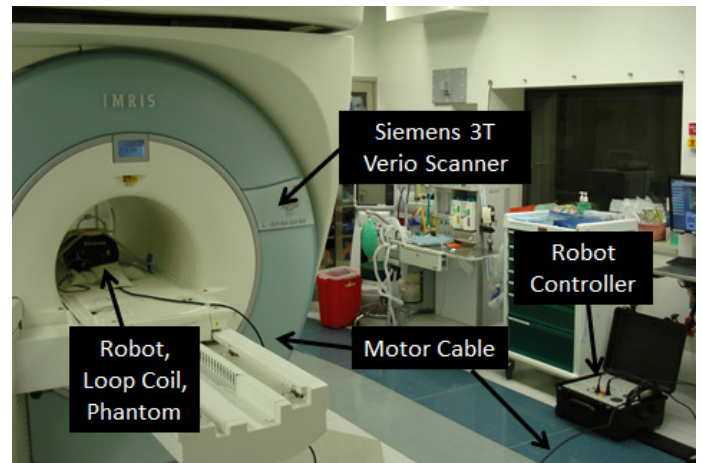


Figure 14. MRI COMPATIBILITY VALIDATION WAS PERFORMED IN A SIEMENS 3T VERIO MR SCANNER.

Three imaging protocols most commonly used for MR image-guided cryoablation, HASTE MBH, 3D VIBE, and T2 TSE, were selected for the compatibility evaluation. Scanning details such as field of view (FV, mm), repetition time (RT, ms), echo time (ET, ms), flip angle (FA, deg), and bandwidth (BW, Hz/pixel) can be found in Tab. 1. Four robot configurations were tested for comparison purposes, including phantom baseline, robot without motor modules, robot with motors off, and robot with motors running. Forty slices, 3 mm thick each, were obtained per imaging protocol for each configuration.

Table 1. SCAN PARAMETERS AND SNR CHANGE COMPARED TO BASELINE

Scan	FV	ET	RT	FA	BW	SNR Base	Motor On, % change
HASTE MBH	85	198	1000	147	504	2.04	2.13, 4.06%
3D VIBE	100	1.68	5.26	10	501	24.9	24.87, 0.22%
T2 TSE	80	106	6944	140	252	2.83	2.77, 2.26%

Figure 15 illustrates the MR images obtained from baseline and during motor operation. The pixel difference between the two images shows small amount of identifiable noise and distortion inside the phantom. The signal to noise ratio (SNR) was calculated as the mean pixel intensity in the center of the phantom divided by the noise intensity (root mean square signal intensity) outside the phantom. As can be observed in Tab. 2, the maximum change in normalized SNR for motor running condition is 4.06% compared to the baseline. This is sufficiently small to not interfere with the operation. MRI compatibility tests conducted with similar controller and actuators can be also found in [27], which reported comparable change in SNR (2.1%).

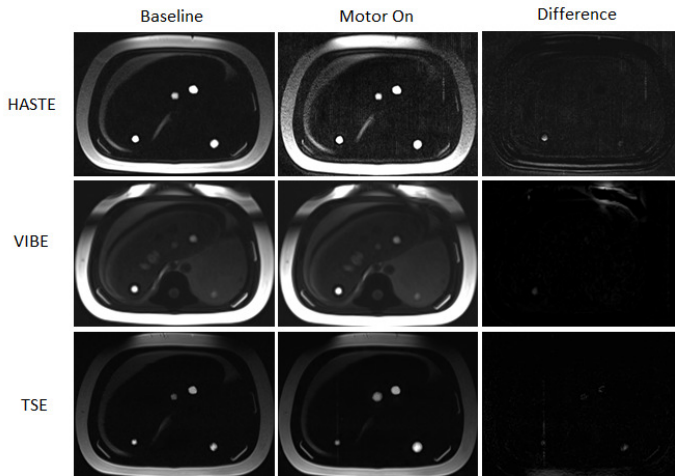


Figure 15. SUBTRACTION NOISE ANALYSIS SHOWS SMALL AMOUNT OF PIXEL DIFFERENCE BETWEEN BASELINE AND MOTOR RUNNING CONDITIONS.

Figure 16 depicts the bench level test setup with a 6-DOF electromagnetic (EM) tracker system (Ascension Tech, Milton, VT) to evaluate the angular accuracy of the arc and the carriage.

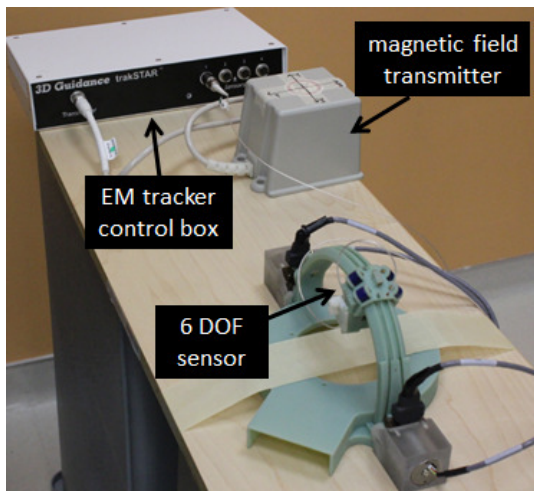


Figure 16. EXPERIMENTAL SETUP WITH A 6-DOF EM TRACKER SYSTEM TO EVALUATE BENCH LEVEL DEVICE PERFORMANCE

The system's repeatability was measured by moving the arc and the carriage independently to a commanded position approaching from either direction. Figure 17 represents bi-directional performance over six trials for each commanded position: three in the forward direction and three in the reverse direction. The extreme angles ($\pm 45^\circ$) can only be approached from one direction; hence only three values are available. The mean of the data corresponds to the accuracy of the system.

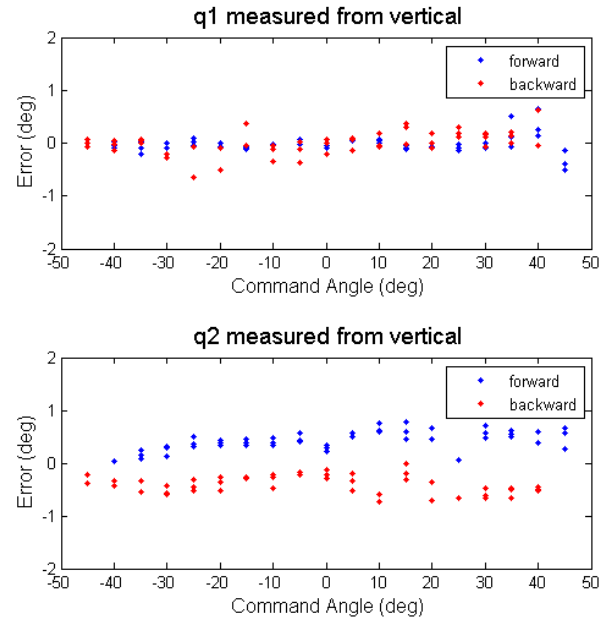


Figure 17. DEVICE PERFORMANCE MEASURED WITH EM TRACKER SYSTEM. THE TOP PLOT IS THE ARC ERROR AND THE BOTTOM PLOT IS THE CARRIAGE ERROR.

Table 2 summarizes the test results. The arc shows consistent behavior as it moves in both directions. The maximum arc error is found to be -0.65° . The slightly larger arc error in the reverse direction, which may be caused by the asymmetrical shape and load of the carriage, would not affect targeting accuracy since only forward movement (clockwise about x-axis) is required during probe placement. The carriage exhibited more overall error, with a maximum of 0.78° . Tensioning the cable prior to the test may improve the carriage performance. With an average probe insertion depth of 125 mm, the angular errors translate to a probe tip error of 2.2 mm.

Table 2. BENCH-LEVEL DEVICE CHARACTERIZATION

	Forward	Backward
Arc (q_1)	$-0.02^\circ \pm 0.17^\circ$	$-0.02^\circ \pm 0.25^\circ$
Carriage (q_2)	$0.43^\circ \pm 0.18^\circ$	$-0.41^\circ \pm 0.17^\circ$

Finally, targeting accuracy of the device was evaluated in gelatin to simulate probe placement in tissue. To register the coordinate system of the EM tracker to the coordinate system of the robot, two EM sensors were secured to the base of the device, as shown in Fig. 18. An additional EM sensor was

installed on the tip of the needle to track its movement within the gelatin. The needle used for the targeting test was a hollow Nitinol tube, which is compatible with the EM field. Figure 19 shows the results of a test in gelatin with 8 targets shaping a “folded star.” The targets were reached using all three needle tracks. The dotted and solid lines show the desired and actual patterns respectively while the maximum error never exceeded 5 mm. The measured targeting errors, $2.0 \text{ mm} \pm 1.5 \text{ mm}$, are larger than the previously calculated 2.2 mm, which may be caused by insertion depth error and needle’s bending in gelatin. A CT-compatible spherical mechanism for positioning a single probe also reported similar results ($2.3 \text{ mm} \pm 1.3 \text{ mm}$) [28].

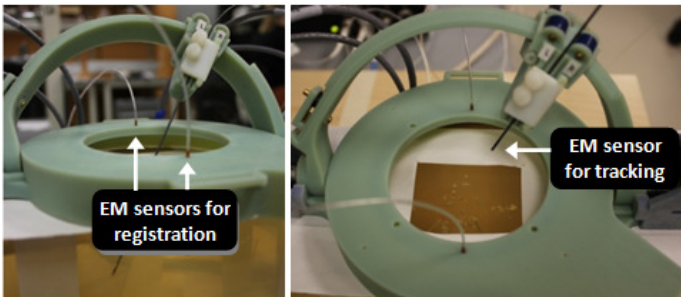


Figure 18. EXPERIMENTAL SETUP WITH 6-DOF EM SENSORS TO REGISTER THE COORDINATE SYSTEMS AND TRACK THE NEEDLE’S TIP IN GELATIN.

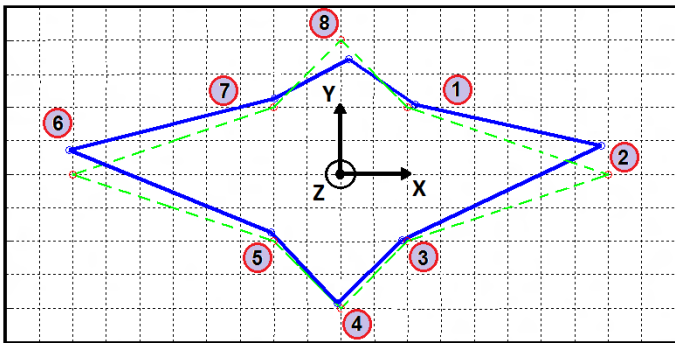


Figure 19. TARGETING RESULTS FROM EXPERIMENTS PERFORMED IN GELATIN (GRID SHOWN IN CM INTERVAL). THE PLANNED PATTERN IS SHOWN WITH DOTTED LINES, AND THE ACTUAL PATTERN IS SHOWN WITH SOLID LINES. ERROR VARIES FROM 0.9 MM TO 4.5MM FOR THE 8 TARGETS.

CONCLUSION AND FUTURE WORK

The 3D printed prototype is a proof of concept for positioning multiple probes for MR-image-guided percutaneous interventions. Such a novel device offers a practical and cost-effective approach to improving the placement of multiple ablation probes to match a treatment plan. The device becomes part of the procedural work-flow as it is mounted together with the MR image coil on the patient. The two actuators are integrated into reusable modules that snap into a single-use or sterilizable base to help maintain a sterile field.

Future work includes verifying the reliability of each

component and optimizing the design. Shielding the actuator modules will further reduce change in SNR. Probe insertion experiments in a phantom model inside an MRI machine are planned and will yield additional useful information for improving the cryoablation work-flow when a robotic positioner is used. Tests need to be performed to guarantee safety before an automated insertion mechanism or steerable ablation probe can be incorporated to further simplify probe positioning and account for probe deflection in tissue. Ultimately, this robot is envisioned to perform automatic probe placement and ablation inside any medical imaging machine, enabling faster, safer, and more economical interventions.

ACKNOWLEDGMENTS

This work is funded by the Partners Radiology Research Award and the Wyss Institute for Biologically Inspired Engineering. We would like to thank the Singapore Ministry of Education through the collaboration between MIT and the Singapore University of Technology and Design. Also, thanks to Greg Cole, Kevin Harrington, and Hao Su from the Automation and Interventional Medicine Lab at WPI for the assistance in learning how to use the motor controller.

REFERENCES

- [1] Gage, A.A., 1998, "History of cryosurgery," *Semin Surg Oncol.*, **14**, pp. 99 -109.
- [2] Lindsey, H., 2007, "Percutaneous Cryoablation Effective for Select Patients with Kidney Tumors," *Oncology Times*, **29** (11), pp. 35-36.
- [3] Georgiades, C.S., Hong, K., Bizzell, .C, Geschwind, J.F., Rodriguez, R., 2008, "Safety and Efficacy of CT Guided Percutaneous Cryoablation for Renal Cell Carcinoma," *JVIR*, **9**, pp. 1302-1310.
- [4] Allaf, M.E., Varkarakis, I.M., Bhayani, S.B., Inagaki, T., Kavoussi, L.R., Solomon, S.B., 2005, "Pain control requirements for percutaneous ablation of renal tumors: cryoablation versus radiofrequency ablation—initial observations," *Radiology*, **237**(1), pp. 366–370.
- [5] Kunkle, D.A., Uzzo, R.G., 2008, "Cryoablation or radiofrequency ablation of the small renal mass: a meta-analysis," *Cancer*, **113**(10), pp. 2671–2680.
- [6] Hegarty, N.J., Gill, I.S., Desai, M.M., Remer, E.M., O'Malley, C.M., Kaouk, J.H., 2006, "Probe-ablative nephron-sparing surgery: cryoablation versus radiofrequency ablation," *J Urol*, **68**(1 suppl), pp. 7–13.
- [7] Permpongkosol, S., Nicol, T.L., Khurana, H., et al., 2007, "Thermal maps around two adjacent cryoprobes creating overlapping ablations in porcine liver, lung, and kidney," *J Vasc Interv Radiol*, **18**(2), pp. 283–287.
- [8] Weld, K.J., Hruby, G., Humphrey, P.A., Ames, C.D., Landman, J., 2006, "Precise characterization of renal parenchymal response to single and multiple cryoablation probes," *J Urol*, **176**(2), pp. 784–786.

- [9] Chosy, S.G., Nakada, S.Y., Lee, F.T. Jr., Warner, T.F., 1998, "Monitoring renal cryosurgery: predictors of tissue necrosis in swine," *J Urol*, **159**(4), pp. 1370–1374.
- [10] Deisenhofer, I., et al., 2010, "Cryoablation versus radiofrequency energy for the ablation of atrioventricular nodal reentrant tachycardia (the CYRANO Study): results from a large multicenter prospective randomized trial," *Circulation*, **122**(22), pp. 2239–45.
- [11] Walsh, c., Sapkota, B., Kalra, M., Hanumara, N., Liu, B., Shepard, J., Gupta, R., 2011, "Smaller and Deeper Lesions Increase Radiation Dose and Time in during Trajectory Planning and Needle Insertion in CT-Guided Lung Biopsy," *J. Thorac Imaging*, **26**(3), pp. 196–203.
- [12] Taillant, N., Avila-Vilchis, J.C., Allegrini, I.B., Cinquin, P., 2004, "CT and MR compatible light puncture robot: architectural design and first experiments," *Proc. 2004 Int'l Soc. & Conf. Series on Med Image Computing and Computer-Assisted Intervention*, Vol. 2, pp. 145–154.
- [13] Hata, N., Tokuda, J., Hurwitz, S., Morikawa, S., 2005, "Needle Guiding Robot for MR-guided Microwave Thermo-therapy of Liver Tumor using Motorized Remote-Center-of-Motion Constraint in Robotics and Automation," *Proc. 2005 IEEE Int'l Conf. Automation and Robotics*, Barcelona.
- [14] Larson, B.T., Erdman, A.G., Tsekos, N.V., Yacoub, E., Tsekos, P.V., Koutlas, I.G., 2004, "Design of an MRI-Compatible Robotic Stereotactic Device for Minimally Invasive Interventions in the Breast," *J. Biomech. Engr*, **126**(4), pp. 458–465.
- [15] Kokes, R., Lister, K., Gullapalli, R., Zhang, B., MacMillan, A., Richard, H., Desai, J., 2009, "Towards a teleoperated needle driver robot with haptic feedback for RFA of breast tumors under continuous MRI," *Med. Image Anal.*, **13**(3), pp. 445 – 55.
- [16] Rasmus, M., Dziergwa, S., Haas, T., Madoerin, P., Huegli, R., Bilecen, D., Jacob, A.L., 2007, "Preliminary clinical results with the MRI-compatible guiding system INNOMOTION," *Int J CARS*, **2**, pp. 138 -145.
- [17] Muntener, M., Patriciu, A., Petrisor, D., Mazilu, D., Bagga, H., Kavoussi, L., Cleary, K., Stoianovici, D., 2006, "Magnetic Resonance Imaging compatible robotic system for fully automated brachytherapy seed placement," *J Urol*, **68**(6), pp. 1313–1317.
- [18] Su, H., Camilo, A., Cole, G.A., Hata, N., Tempany, C.M., Fischer, G.S., 2011, "High-field MRI-compatible needle placement robot for prostate interventions," *Stud Health Technol Inform*, **163**, pp. 623–629.
- [19] Walsh, C., Hanumara, N., Slocum, A., Shepard, J., Gupta, R., 2008, "A patient-mounted telerobotic tool for CT-guided percutaneous interventions," *ASME Journal of Medical Devices*, **2**(1).
- [20] Wu, F., 2013, "Multi-probe robotic positioner for cryoablation in MRI," SMME Thesis, MIT, Cambridge, MA, USA.
- [21] Slocum, A.H., 1992, *Precision Machine Design*, Society of Manufacturing.
- [22] Fischer, G.S., Krieger, A., Iordachit, I., Csoma, C., Whitcomb, L., Fichtinger, G., 2008, "MRI Compatibility of Robot Actuation Techniques – A Comparative Study," *MICCAI 2008*, Part II, LNCS 5242, pp. 509–517.
- [23] Wang, Y., Shazeeb, M.S., Sotak, C.H., Fischer, C.S., 2009, "Optimization of Piezoelectric Motors to Enhance MR Compatibility for Interventional Devices," *17th Sci. Meeting and Exhibition of the Int'l Soci. of Mag. Reso. in Med. - ISMRM 2009*.
- [24] Verdirame, J., 2000, "Characterization of a Hydraulic Actuator for a Functional Magnetic Resonance Imaging Robot," BSME Thesis, MIT, Cambridge, MA, USA.
- [25] Stein, H. L., 1998, "Ultrahigh molecular weight polyethylenes (uhmwpe)," *Engineered Materials Handbook*, **2**, 167–171.
- [26] Cole, G., Harrington, K., Su, H., Camilo, A., Pilitis, J., Fischer, G.S., 2010, "Closed-Loop Actuated Surgical System Utilizing Real-Time In-Situ MRI Guidance," *12th Int'l Symp. on Expe. Robotics - ISER 2010*
- [27] Wang, Y., Cole, G.A., Su, H., Pilitis, J.G., Fischer, G.S., 2009, "MRI Compatibility Evaluation of a Piezoelectric Actuator System for a Neural Interventional Robot," *31st Annual Int'l Conf. of the IEEE Engr. Med. and Bio. Soci. - EMBC 2009*, Minneapolis, MI.
- [28] Maier-Hein, L., Walsh, C., Seitel, A., Hanumara, N., Shepard, J., Pianka, F., Muller, B., Slocum, A., Gupta, R., Meinzer, H-P., 2009, "Human vs. Robot Operator Error in a Needle-Based Navigation System for Percutaneous Liver Intervention," *Proc. SPIE*, vol. 7261, pp. 72610Y-72610Y-12.